

# Halo spin and orientation in Interacting Dark Matter Dark Energy Cosmology

Guandi Zhao\*

*Department of Physics, ETH Zurich, 8092 Zurich, Switzerland*

Jiajun Zhang,<sup>†</sup> Peng Wang, and Ji Yao

*Shanghai Astronomical Observatory, Chinese Academy of Sciences, Shanghai 200030, China*

(Dated: January 8, 2025)

In recent years, the interaction between dark matter (DM) and dark energy (DE) has become a topic of interest in cosmology. Interacting dark matter–dark energy (IDE) models have a substantial impact on the formation of cosmological large-scale structures, which serve as the background for DM halo evolution. This impact can be examined through the shape and spin orientation of halos in numerical simulations incorporating IDE effects. In our work, we used the N-body simulation pipeline **ME-GADGET** to simulate and study the halo spin and orientation in IDE models. We found that in models where DM transfers into DE (IDE I), the alignment of halo shapes with the surrounding tidal field is enhanced, while the alignment of halo spins with the tidal field is decreased compared to the  $\Lambda$ CDM. Conversely, in models where DE transfers into DM (IDE II), the opposite occurs. We have provided fitted functions to describe these alignment signals. Our study provides the foundation for more accurate modeling of observations in the future such as China Space Station Telescope (CSST).

## I. INTRODUCTION

The accelerating expansion of the current universe implies the presence of a component with negative pressure, identified as Dark Energy (DE)<sup>1</sup>.  $\Lambda$ CDM model assumes constant dark energy density ( $\Lambda$ ), and is supported by observations of both the early and late universe, such as Cosmic Microwave Background (CMB)<sup>2–4</sup>, Baryonic Acoustic Oscillations (BAO)<sup>5,6</sup>, as well as the observation of the later universe by type Ia Supernova (SNIa)<sup>1,7</sup>.

However,  $\Lambda$ CDM model is challenged by recent observations, especially the Hubble tension and the S8 tension<sup>8–12</sup>. The Hubble tension is a discrepancy between indirect measurements of early universe, such as CMB and BBN and direct constraints based on local distance ladder<sup>3,5,6,13</sup>, and S8 tension is the discrepancy between matter anisotropy measured by CMB and the matter clustering strength measured by weak lensing experiments<sup>12,14–18</sup>.

Besides, Recent results from the DESI collaboration, combining DESI (FS+BAO), CMB, and DES-SN5YR data<sup>19,20</sup>, provide evidence for a dynamical dark energy equation of state (EoS) ( $\omega_0\omega_a$  CDM model), parameterized by  $\omega(a) = \omega_0 + (1 - a)\omega_a$  with posterior  $\omega_0 = -0.761 \pm 0.065$  and  $\omega_a = -0.96^{+0.30}_{-0.26}$ . This suggests that dark energy may have varying ratio between mass and pressure over the evolution of the universe.

Interacting dark energy dark matter (IDE) models provide a framework to explain the evolution of the dark energy EoS and have acquired academic interest. Besides, IDE models offer a potential solution to the  $H_0$ -S8 tension<sup>21–25</sup>. In the future, observations conducted by telescopes such as China Space Station Telescope (CSST) may provide key evidence through weak lensing<sup>26</sup>. A more precise modeling of observational signals is necessary.

To constrain the IDE models more precisely, we need

cosmological simulations to make observational predictions and look for potential hints for DM-DE interactions. Baldi et. al.<sup>27</sup> first examined the effects of IDE in nonlinear matter power spectrum using N-body simulation. In 2018, Zhang et al.<sup>28</sup> adopted **ME-GADGET** (a modified version of the **GADGET-2**<sup>29–31</sup>), and incorporated IDE effects into DM-only N-body simulation. The result demonstrated that the mass power spectrum difference across IDE models happens after  $z \sim 1$ . In a consecutive paper<sup>32</sup>, Liu et al. examined the halo mass function and the halo  $c_{200} - M_{200}$  relation across IDE models.

Our work adopts the same simulation dataset and convention as Liu et al.<sup>32</sup>, and focuses on the examination of the relation between DM halos and their forming environments across IDE models. In this work, section II covers the theory and simulation approach of this work; section III lists the halo alignment relation across IDE models, section IV discusses the implications of halo alignment relation and possible observational probes.

## II. METHODOLOGY

### A. IDE cosmology

IDE effects on halo formation in two major aspects. Firstly, IDE models yield different cosmic expansion history  $a(t)$  and start time of halo formation is affected; secondly, IDE models modify halo mass and thus their self and mutual gravity. The background expansion history is a modified version of the  $\Lambda$ CDM spacetime with flat FLRW metric:

$$ds^2 = -dt^2 + a^2(t)(dx^2 + dy^2 + dz^2). \quad (1)$$

The 00 component for Einstein field equations gives the first Friedmann equation:

$$\frac{H^2}{H_0^2} = \frac{8\pi G}{3H_0^2}(\rho_M + \rho_E). \quad (2)$$

In this work, we use a phenomenological model to parametrize IDE models based on 0th component energy-momentum transfer  $Q = Q^0$ ,

$$\nabla_\mu T_M^{\mu\nu} = Q^\nu, \quad (3)$$

$$\nabla_\mu T_E^{\mu\nu} = -Q^\nu. \quad (4)$$

taking the leading order contribution to  $Q$  from  $\rho_M$  and  $\rho_E$ , the transfer is parametrized as  $Q(H, \rho_M, \rho_E) = \xi_1 \rho_M + \xi_2 \rho_E$ <sup>33,34</sup>.

The matter evolution follows equations 3 and 4, which simplifies into:

$$\dot{\rho}_M + 3H\rho_x = Q, \quad (5)$$

$$\dot{\rho}_E + 3H(\omega_E + 1)\rho_x = -Q, \quad (6)$$

where  $\omega_E$  is the EoS parameter of DE. Following Liu et al.<sup>32</sup> we focus on a specific subset of parameter space that probes the effect of  $\xi_2$ , listed in tableI.

Model	IDE I	$\Lambda$ CDM	IDE II
$\omega_E$	-0.9461	-1	-1.088
$\xi_2$	-0.0738	0	0.05219
$\Omega_b h^2$	0.022237	0.022325	0.02224
$\Omega_m h^2$	0.0927	0.1198	0.1351
$\ln 10^{10} A_s$	3.099	3.094	3.097
$n_s$	0.9645	0.9645	0.9643
$H_0$	68.18	67.27	68.35

TABLE I: Model parameters considered in this work.  $\Lambda$ CDM parameters come from planck collaboration 2015 results<sup>4</sup>). IDE I and IDE II are two set of different best fit values with Planck CMB + BAO + SNIa +  $H_0$  respectively in the domain of  $\omega_E < -1$  and  $\omega_E > -1$ <sup>32,35</sup>.

The expansion history is altered by the IDE energy reansfer, and the matter density evolution deviates from  $\propto a^{-3}$  (as in  $\Lambda$ CDM):

$$\rho_M(a) = \frac{3H_0^2}{8\pi G} \left[ \Omega_M + \frac{\xi_2 \Omega_E}{\xi_2 + \omega_E} (1 - a^{\omega_D + \xi_2}) \right] a^{-3}, \quad (7)$$

indicating the DM particle mass evolve during the simulation of the model IDE I and IDE II, demonstrated in 1. DM particles decay in IDE I while proliferate in IDE II.

## B. N-body simulation for IDE models

In order to predict the large-scale structure configuration at different IDE parameters, we adopt a Dark-Matter-only N-body simulation

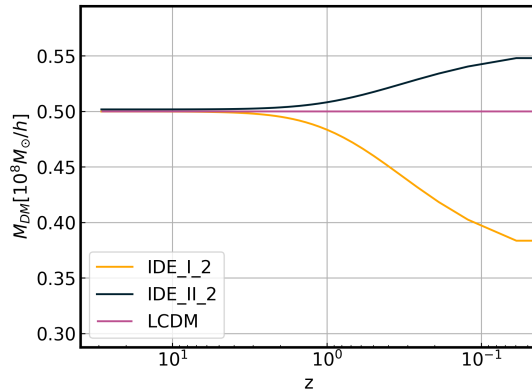


FIG. 1: Mass of DM particles at different redshift in IDE I,  $\Lambda$ CDM and IDE II, respectively. Note that the difference between IDE models and  $\Lambda$ CDM is only significant ( $\sim 1$ ) at  $z < 4$ , which is consistent with the low-redshift property of the DM-DE interaction.

Our work is based on code `ME-GADGET`<sup>28</sup> simulation which establishes a full pipeline to account for IDE effects. The `ME-GADGET` is a modified version of `GADGET-2` code<sup>30,31</sup>. Our simulation box size is  $200 Mpc/h$  with particle number  $512^3$ , with periodic boundary conditions. The halos are identified with Amiga Halo Finder `AHF`<sup>36</sup>. The pre-initial conditions is generated by `CCVT`<sup>37</sup>. The initial power spectrum is generated by a modified version of `CAMB`<sup>38</sup>. The initial condition is generated by a modified version of `2LPTic`<sup>39</sup>.

Due to the difference in total DM mass, the total count of `AHF` halos have a large difference across models. The simulation results in 68125 halos in IDE I model, 200355 halos in  $\Lambda$ CDM and 205238 halos in IDE II model, with their halo mass function shown in Fig.2.

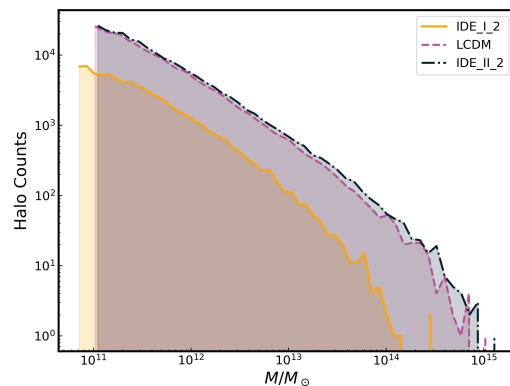


FIG. 2: Halo mass functions in IDE I,  $\Lambda$ CDM, IDE II, respectively. The total number of halos in IDE I is significantly less than  $\Lambda$ CDM due to DM decay.

In order to examine the physical relation between halo

and its forming environment, the angular momentum and shape major axes of halos are computed and normalized to unit vectors.

The definition of angular momentum for each halo is:

$$\vec{L}_{halo} = \sum_{i \in halo} m_i \vec{v}'_i \times \vec{r}'_i. \quad (8)$$

And the shape orientation is characterized by the major axes of the inertia tensor:

$$\overleftrightarrow{I}_{halo} = \sum_{i \in halo} m_i \vec{r}'_i \vec{r}'_i \quad (9)$$

$$\overleftrightarrow{I}_{halo} = \sum_{\alpha=a,b,c} I_\alpha \vec{e}_\alpha \vec{e}_\alpha \quad (10)$$

with  $I_c < I_b < I_a$ , and  $\vec{e}_a, \vec{e}_b, \vec{e}_c$  perpendicular to each other.

Within the scope of our study, we focus primarily on the primary major axis  $\vec{G} = \vec{e}_a$  because it characterizes the most elongated direction of the halo in the gravitational environment.

### C. Tidal field eigendirections

We expect the halo spin and shape to be largely affected by the tidal force. Therefore, it is interesting to investigate the tidal field around halos.

In the  $\Lambda$ CDM model, the formation of halos follows a 'sheet-filament-cluster' migration pattern, and an alignment between the halo spin to the cosmic environment shows that halos at redshift zero with  $M_{vir} > 10^{11} M_\odot$  have spin direction statistically perpendicular to the tidal field eigendirection<sup>40</sup>.

Thus, in order to compare the effects of IDE on the halo shape and major axis, we need to introduce the tidal field eigendirections.

The tidal field is computed by definition  $T_{ij} = \partial_i \partial_j \Phi$ <sup>41,42</sup>. With the gravitational potential field  $\Phi$  calculated by the Poisson equation:

$$\nabla^2 \Phi = 4\pi G \rho. \quad (11)$$

Numerically, the mass assignment used the cloud-in-cell (CIC) method from the `Pylians`<sup>43</sup> package. The assigned 3d mass grid has a spacing of  $0.781 Mpc/h$ . The smoothing was carried out in Fourier space with a smoothing radius of  $R_s = 2 Mpc/h$

The smoothed density field was then convolved with the 3D green's function to obtain the gravitational potential field:

$$\Phi(\vec{r}) = - \int d^3 r' \frac{\rho(\vec{r}')}{|\vec{r} - \vec{r}'|}. \quad (12)$$

The tidal shear tensor is the traceless part of the hessian matrix of the gravitational potential field:

$$T_{ij} = \sum_{i,j} \partial_i \partial_j \Phi_{ij} - \frac{1}{3} \sum_i \partial_i^2 \Phi \quad (13)$$

The tidal field direction  $\vec{T}_3$  ( $\vec{T}$  in the following) is the eigenvector of  $T_{ij}$  with the least eigenvalue. This direction also corresponds to the direction where dark matter collapses the least in linear perturbation theories.

In our simulations, the tidal eigenvectors are demonstrated in the third row of Fig.3. To compare the halo shape alignment and spin alignment across models, we examine the in-situ correlation in III B and III C and the alignment correlation function in III D.

In Fig.3, comparing the second row to the third row, we can see at filamentary structures, the tidal field follows the direction of filaments. At filaments,  $\vec{T}_3$  points towards the direction of the filament within the perspective plane (colored in dark blue), and at filament nodes,  $\vec{T}_3$  points above the perspective plane.

## III. RESULT

We have seen the tidal field and halo distribution in Fig.3. Here we proceed to quantitatively analyze the spin-tidal correlation, shape-tidal correlation and their autocorrelations. It is interesting to see if the relations are affected by DM-DE interactions.

### A. Alignment Strength

Before introducing the in-situ correlation and the alignment correlation function, we define the alignment strength of 3d vectors: for two halos pointing at unit vectors  $\vec{v}_1$  and  $\vec{v}_2$ , the alignment strength is defined as:

$$\eta_{12}^{(3)} = (\vec{v}_1 \cdot \vec{v}_2)^2 - 1/3, \quad (14)$$

where the 1/3 factor is to ensure that for a (spherically symmetric) random distribution of 3D unit vectors, the expectation value for the alignment strength is 0. A positive alignment strength means two vectors tend to align, while a negative alignment strength means two vectors tend to be perpendicular.

This alignment definition is invariant under the inversion of either one of the vectors. The definition is chosen due to the arbitrariness of choice for the positive direction of the tidal eigenvector  $\vec{T}_3$  and the primary major axis  $\vec{G}$ .

### B. Spin-tidal in-situ correlation

In  $\Lambda$ CDM, the halo spin-tidal alignment depends on halo mass, with the alignment switching from positive to negative at  $M_{halo} \sim 10^{12} M_\odot$ <sup>40</sup>. Here we expect a similar behavior for IDE models. To analyze deviations from  $\Lambda$ CDM, in IDE models, we compare alignment strengths across mass bins ranging from  $10^{11} M_\odot$  to  $10^{13} M_\odot$ .

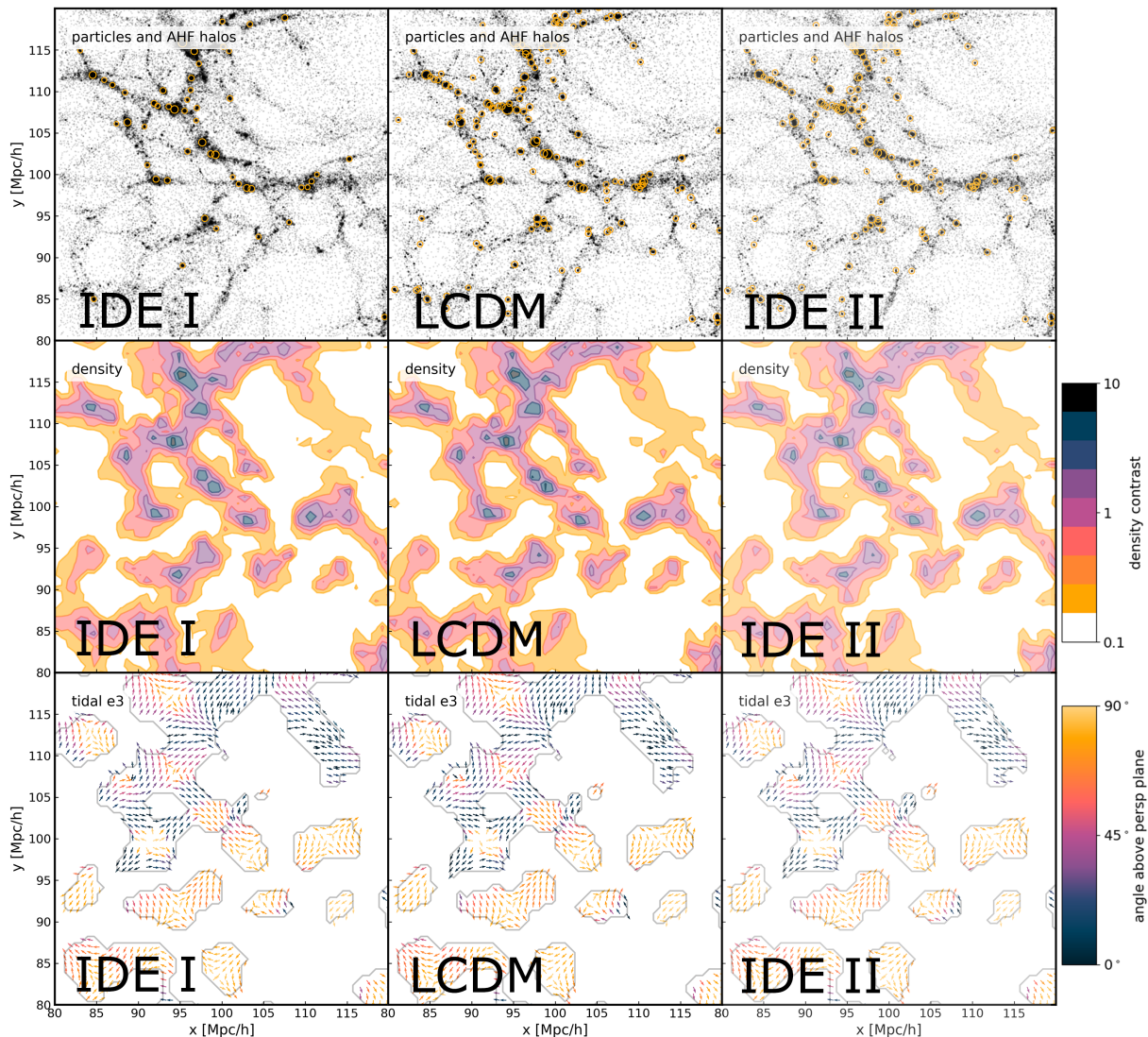


FIG. 3: The figure shows simulated particle snapshots (first row), density heightmap (second row), and the tidal field direction  $\vec{T}_3$  (third row) in models IDE I,  $\Lambda$ CDM and IDE II. First row: the simulation particle snapshots at redshift 0 (black point cloud), and the AHF halos (orange circles with radius representing the virial radius  $R_{vir}$ ). Second row: density heatmap at overdensity  $\delta > 0$ . Third row: the tidal tensor least eigenvalue arrow plot in dense regions, with coloring denoting the inclination angle above the perspective plane.

We show the unbinned distribution of  $\cos \theta_{GT}$  in Fig. 4, showing that compared to  $\Lambda$ CDM model, IDE (IDE II) show less (more) spin-shape alignment.

The spin-tidal relation with halo mass is shown in Fig. 5. Note that the y-axis value is positive (negative) when shape-tidal directions tend to be parallel (perpendicular). In all three models, alignment strength generally decreases with halo mass, and the crossing happens at  $\sim 10^{12} h^{-1} M_{\odot}$  in  $\Lambda$ CDM, consistent with the results from Wang et al.<sup>40</sup>. This means smaller (massive) halos tend to have spin parallel (perpendicular) to the tidal field. The IDE I model has fewer mass bins due to its fewer total halo counts. The linear best-fit parameters are listed in Table II. The fitting parameter shows a significant ten-

dency of perpendicular (parallel) spin-tidal orientation for IDE I (IDE II), compared to  $\Lambda$ CDM model, which is consistent with unbinned results. This implies DM mass decay in IDE I makes the halo spin tend to be perpendicular to the tidal field eigendirection.

### C. Shape-tidal in-situ correlation

In  $\Lambda$ CDM, the halo shape tends to align with the tidal field, which is caused by both tidal forces and feeding mechanisms, resulting in a shape elongated towards tidal eigendirection. To see the effect of IDE on shape-tidal alignment, we carry out a similar analysis as III B and

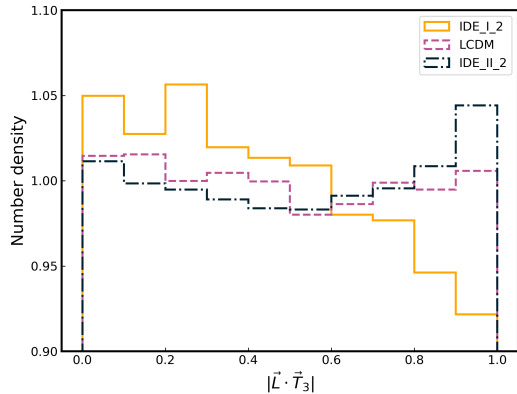


FIG. 4: Vertically zoomed-in histogram of the spin-tidal alignment angle. The horizontal axis is  $|\vec{L} \cdot \vec{T}_3| = \cos \theta_{GT}$ .

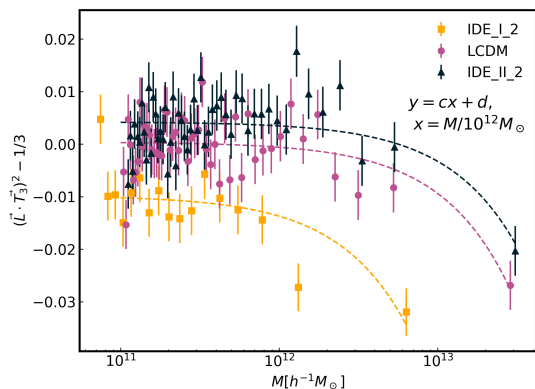


FIG. 5: The figure shows the spin-tidal alignment strength in relation to halo mass. The linear fit is given by the solid-dash lines.

Model	$10^3 c$ (Mean $\pm$ Std)	$10^3 d$ (Mean $\pm$ Std)
IDE I	$-3.88 \pm 0.77$	$-9.83 \pm 1.25$
$\Lambda$ CDM	$-0.98 \pm 0.16$	$0.38 \pm 0.71$
IDE II	$-0.75 \pm 0.15$	$4.22 \pm 0.69$

TABLE II: Linear fit best-fit parameters of spin-tidal alignment for the empirical relation  $y = cx + d$ , where  $x = M/10^{12} M_\odot$ .

compare alignment strengths across mass bins ranging from  $10^{11} M_\odot$  to  $10^{13} M_\odot$ .

We show the relation between shape-tidal alignment and halo mass in Fig.6. In mass range  $10^{11} M_\odot \sim 10^{13} M_\odot$ , alignment between shape and tidal field is positive across three models, which is consistent with our understanding of  $\Lambda$ CDM. A power law fit is given with  $y = ax^b$ , where  $x = M/10^{12} M_\odot$ , and the corresponding fit parameters are listed in Table III. Comparison be-

tween models shows that generically, the shape of IDE I (IDE II) halos more (less) parallel to the tidal field than  $\Lambda$ CDM.

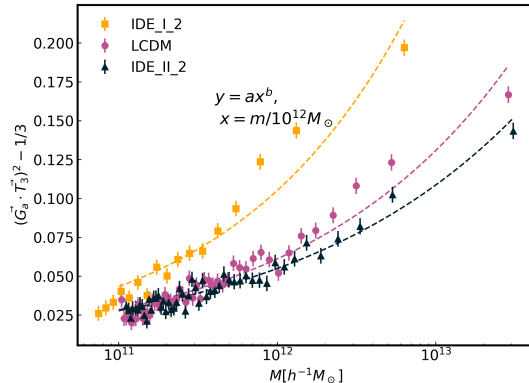


FIG. 6: The figure shows the shape-tidal alignment strength in relation to halo mass. The power-law best fit is given by the solid-dash lines.

Model	$a$ (Mean $\pm$ Std)	$b$ (Mean $\pm$ Std)
IDE I	$0.1051 \pm 0.0016$	$0.3864 \pm 0.0096$
$\Lambda$ CDM	$0.0611 \pm 0.0008$	$0.3307 \pm 0.0070$
IDE II	$0.0549 \pm 0.0008$	$0.2963 \pm 0.0077$

TABLE III: Best fit power-law parameters for the empirical relation  $y = ax^b$ , where  $x = M/10^{12} M_\odot$ .

#### D. Alignment Correlation

From Section III C, there is significantly stronger shape alignment in IDE I and less alignment in IDE II between the halo shape and tidal field. Such halo shape alignment could potentially affect galaxy-galaxy alignment and have observational effects in weak lensing experiments. Thus, autocorrelations between halos at different separations are particularly interesting.

We define the halo alignment correlation as a function of the halo separation. The shape-shape correlation is defined as:

$$\eta^{gg}(r) = \left\langle (\vec{G}(\vec{x}) \cdot \vec{G}(\vec{x}, r, \theta, \phi))^2 - 1/3 \right\rangle_{\vec{x}, \theta, \phi},$$

and the spin-spin correlation is defined as:

$$\eta^{ll}(r) = \left\langle (\vec{L}(\vec{x}) \cdot \vec{L}(\vec{x}, r, \theta, \phi))^2 - 1/3 \right\rangle_{\vec{x}, \theta, \phi}.$$

Using the halo catalog generated by AHF as discussed in II B, we find all halo pairs with separation in the range  $[0.1, 20.0] Mpc/h$ . Due to the inaccuracy of angular momentum calculation at lower particle counts, only halos with  $N_{part} > 10^2$  are considered.

In Fig.7, we show the shape-shape autocorrelation and in Fig9, we show the spin-spin autocorrelation. Cross correlations between shape, spin and tidal vectors are shown in Fig. 10, Fig. 8, and Fig. 11. The tidal field autocorrelation is not shown due to insignificant difference across models.

In IDE I, a stronger correlation in shape-shape and shape-tidal is shown in Fig. 7 and Fig. 8, while for IDE II the correlation is slightly weaker than  $\Lambda$ CDM due to the small value of  $\xi_2$ . This is consistent with what we found in Fig. 6 and Fig. 5. Since the tidal field autocorrelation shows little difference across models, the stronger shape-shape and shape-tidal correlation in IDE I is the result of the shape of halos following the direction of tidal field.

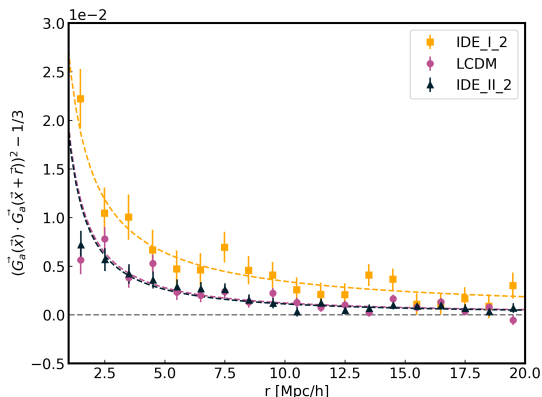


FIG. 7: This figure shows the autocorrelation of shape-shape with respect to the separation distance of halos in  $Mpc/h$ . The solid-dash lines present the powerlaw best-fit line, with parameters shown in Table IV.

Model	$a$ (Mean $\pm$ Std)	$b$ (Mean $\pm$ Std)
IDE I	$0.0310 \pm 0.0024$	$-0.974 \pm 0.059$
$\Lambda$ CDM	$0.0188 \pm 0.0012$	$-1.134 \pm 0.053$
IDE II	$0.0192 \pm 0.0012$	$-1.192 \pm 0.056$

TABLE IV: Fitting parameters for the empirical relations shown in Fig. 7, with relation  $y = ar^b$  and  $r$  in the unit of  $Mpc/h$ .

Model	$10^5 a$ (Mean $\pm$ Std)	$10^4 b$ (Mean $\pm$ Std)	$c$ (Mean $\pm$ Std)
IDE I	$3.31 \pm 0.82$	$-2.04 \pm 0.08$	$-4.59 \pm 0.35$
$\Lambda$ CDM	$1.89 \pm 0.62$	$-1.98 \pm 0.10$	$-4.25 \pm 0.44$
IDE II	$1.02 \pm 0.40$	$-1.84 \pm 0.11$	$-3.42 \pm 0.47$

TABLE V: Fitting parameters for the empirical relations shown in Fig. 8, with relation  $y = a(r - c)^b$  and  $r$  in the unit of  $Mpc/h$ .

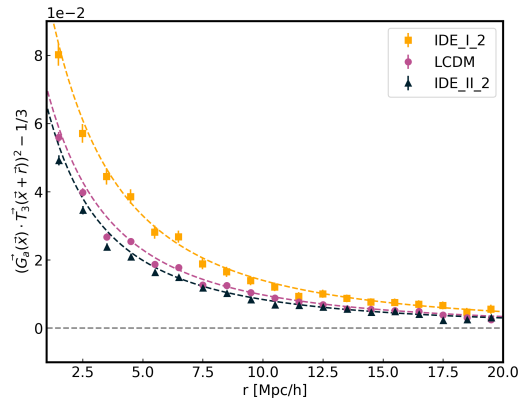


FIG. 8: This figure shows the crosscorrelation of tidal-shape with respect to the separation distance of halos in  $Mpc/h$ . The solid-dash lines present the shifted powerlaw best-fit line, with parameters shown in Table V.

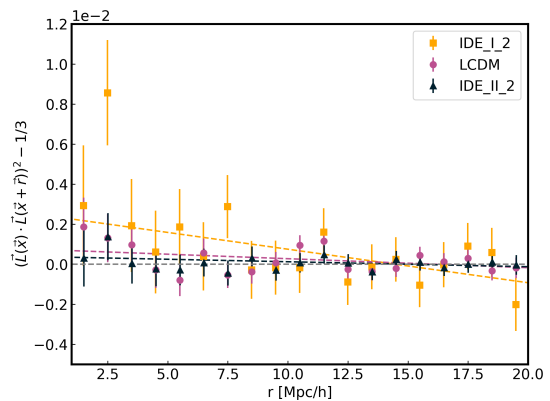


FIG. 9: This figure shows the autocorrelation of spin-spin with respect to the separation distance of halos in  $Mpc/h$ . The solid-dash lines present the linear best-fit line, with parameters shown in Table VI.

Model	$10^5 a$ (Mean $\pm$ Std)	$10^4 b$ (Mean $\pm$ Std)
IDE I	$-16.8 \pm 6.8$	$24.3 \pm 9.1$
$\Lambda$ CDM	$-4.5 \pm 2.9$	$7.2 \pm 3.9$
IDE II	$-2.5 \pm 2.7$	$3.7 \pm 3.8$

TABLE VI: Fitting parameters for the empirical relations shown in Fig. 9, with relation  $y = ar + b$  and  $r$  in the unit of  $Mpc/h$ .

#### IV. CONCLUSION AND DISCUSSION

This study compares dissipative and proliferating IDE models (IDE I and IDE II) in terms of halo properties, specifically the correlation between halo spin, shape, and

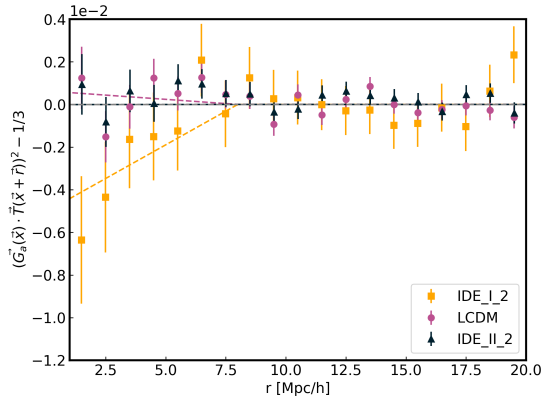


FIG. 10: This figure shows the crosscorrelation of shape-spin with respect to the separation distance of halos in  $Mpc/h$ . The solid-dash lines present the broken-linear best-fit line, with parameters shown in Table VII.

Model	$10^5 a$ (Mean $\pm$ Std)
IDE I	$63 \pm 21$
$\Lambda$ CDM	$-8.0 \pm 9.8$
IDE II	$0.0 \pm 9.5$

TABLE VII: Fitting parameters for the empirical relations shown in Fig. 10, with relation  $y = a(r - 8)[r < 8]; y = 0[r \geq 8]$  and  $r$  in the unit of  $Mpc/h$ .

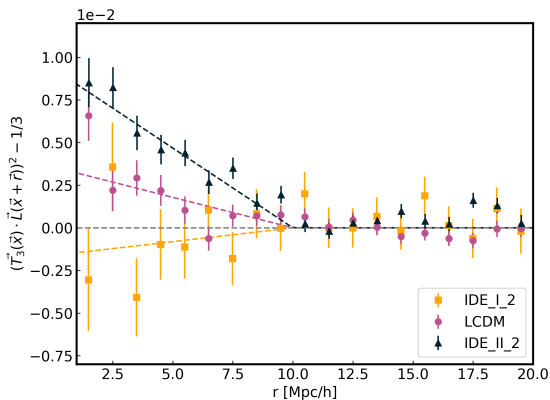


FIG. 11: This figure shows the crosscorrelation of tidal-spin with respect to the separation distance of halos in  $Mpc/h$ . The solid-dash lines present the broken-linear best-fit line, with parameters shown in Table VIII.

the surrounding tidal field.

We find that there are fewer halos with spin aligned to the tidal field and more halos with shape aligned to the tidal field in the dissipative IDE model. In contrast,

Model	$10^4 a$ (Mean $\pm$ Std)
IDE I	$1.6 \pm 1.3$
$\Lambda$ CDM	$-3.6 \pm 0.6$
IDE II	$-9.4 \pm 0.6$

TABLE VIII: Fitting parameters for the empirical relations shown in Fig. 11, with relation  $y = a(r - 10)[r < 8]; y = 0[r \geq 10]$  and  $r$  in the unit of  $Mpc/h$ .

proliferating IDE models show the opposite trend, with more halos having spin aligned to the tidal field and fewer halos with shape aligned. This difference in shape-tidal alignment results in the shape-shape autocorrelation significantly enhanced in dissipative IDE, while it is mildly reduced in proliferating IDE.

We highlight the following conclusions we find in the study:

- Spin-tidal alignment: stronger in IDE II, weaker in IDE I, as demonstrated in Fig. 5.
- Shape-tidal alignment: stronger in IDE I, weaker in IDE II, as demonstrated in Fig. 6.
- Shape-shape: significantly stronger in IDE I and weaker in IDE II, as demonstrated in the Fig. 7.
- Spin-spin: insignificant difference across IDE models.

The effect of higher (lower) shape-tidal and shape-shape correlation in dissipative (proliferating) IDE models can be explained by the difference in density profile. Liu et al<sup>32</sup>. found that the halo concentrations  $c_{200}$  in dissipative IDE models are lower and halos are more eccentric than in proliferating IDE and  $\Lambda$ CDM. This makes halos in dissipative IDE more sensitive to environmental effects from the tidal field, leading to stronger shape-tidal and shape-shape correlations.

To account for the effect of lower spin-tidal correlation seen in Fig. 5, we postulate that, in dissipative IDE, the halos at  $z=0$  could only have survived the mass decay and halo disassembly by accreting material from dense regions (clusters and filaments). As Wang et al. discussed, the halo migration while staying within the filament helps gain angular momentum perpendicular to tidal eigendirection<sup>40</sup>, which means smaller mass halos in dissipative IDE corresponds to more massive halos in  $\Lambda$ CDM that stays extended periods inside filaments.

Our findings provide the ingredients for more precise modeling in terms of weak lensing for future observations like China Space Station Telescope (CSST).

## V. ACKNOWLEDGEMENT

This work was supported by National Natural Science Foundation of China (NSFC) grants 12473003 and

the China Manned Space Project with no. CMS-CSST-2021-A03. JY acknowledges the support from National Natural Science Foundation of China (NSFC) grants 12203084. PW acknowledge the support from

National Natural Science Foundation of China (NSFC) grants 12473009 and Shanghai Rising-Star Program No. 24QA2711100. This work was inspired by the discussion in HOUYI workshop held in Shanghai, 2023.

\* guzhao@ethz.ch

† jjzhang@shao.ac.cn

- <sup>1</sup> Adam G. Riess, Alexei V. Filippenko, Peter Challis, Alejandro Clocchiatti, Alan Diercks, Peter M. Garnavich, Ron L. Gilliland, Craig J. Hogan, Saurabh Jha, Robert P. Kirshner, B. Leibundgut, M. M. Phillips, David Reiss, Brian P. Schmidt, Robert A. Schommer, R. Chris Smith, J. Spyromilio, Christopher Stubbs, Nicholas B. Suntzeff, and John Tonry. Observational Evidence from Supernovae for an Accelerating Universe and a Cosmological Constant. *AJ*, 116(3):1009–1038, September 1998.
- <sup>2</sup> E. Komatsu, K. M. Smith, J. Dunkley, C. L. Bennett, B. Gold, G. Hinshaw, N. Jarosik, D. Larson, M. R. Nolta, L. Page, D. N. Spergel, M. Halpern, R. S. Hill, A. Kogut, M. Limon, S. S. Meyer, N. Odegard, G. S. Tucker, J. L. Weiland, E. Wollack, and E. L. Wright. Seven-year Wilkinson Microwave Anisotropy Probe (WMAP) Observations: Cosmological Interpretation. *ApJS*, 192(2):18, February 2011.
- <sup>3</sup> Planck Collaboration, N. Aghanim, Y. Akrami, M. Ashdown, J. Aumont, C. Baccigalupi, M. Ballardini, A. J. Banday, R. B. Barreiro, N. Bartolo, S. Basak, R. Battye, K. Benabed, J. P. Bernard, M. Bersanelli, P. Bielewicz, J. J. Bock, J. R. Bond, J. Borrill, F. R. Bouchet, F. Boulanger, M. Bucher, C. Burigana, R. C. Butler, E. Calabrese, J. F. Cardoso, J. Carron, A. Challinor, H. C. Chiang, J. Chluba, L. P. L. Colombo, C. Combet, D. Contreras, B. P. Crill, F. Cuttaia, P. de Bernardis, G. de Zotti, J. Delabrouille, J. M. Delouis, E. Di Valentino, J. M. Diego, O. Doré, M. Douspis, A. Ducout, X. Dupac, S. Dusini, G. Efstathiou, F. Elsner, T. A. Enßlin, H. K. Eriksen, Y. Fantaye, M. Farhang, J. Fergusson, R. Fernandez-Cobos, F. Finelli, F. Forastieri, M. Frailis, A. A. Fraisse, E. Franceschi, A. Frolov, S. Galeotta, S. Galli, K. Ganga, R. T. Génova-Santos, M. Gerbino, T. Ghosh, J. González-Nuevo, K. M. Górski, S. Gratton, A. Gruppuso, J. E. Gudmundsson, J. Hamann, W. Handley, F. K. Hansen, D. Herranz, S. R. Hildebrandt, E. Hivon, Z. Huang, A. H. Jaffe, W. C. Jones, A. Karakci, E. Keihänen, R. Keskitalo, K. Kiiveri, J. Kim, T. S. Kisner, L. Knox, N. Krachmalnicoff, M. Kunz, H. Kurki-Suonio, G. Lagache, J. M. Lamarre, A. Lasenby, M. Lattanzi, C. R. Lawrence, M. Le Jeune, P. Lemos, J. Lesgourgues, F. Levrier, A. Lewis, M. Liguori, P. B. Lilje, M. Lilley, V. Lindholm, M. López-Cañiego, P. M. Lubin, Y. Z. Ma, J. F. Macías-Pérez, G. Maggio, D. Maino, N. Mandolesi, A. Mangilli, A. Marcos-Caballero, M. Maris, P. G. Martin, M. Martinelli, E. Martínez-González, S. Matarrese, N. Mauri, J. D. McEwen, P. R. Meinhold, A. Melchiorri, A. Mennella, M. Migliaccio, M. Millea, S. Mitra, M. A. Miville-Deschênes, D. Molinari, L. Montier, G. Morgante, A. Moss, P. Natoli, H. U. Nørgaard-Nielsen, L. Pagano, D. Paoletti, B. Partridge, G. Patanchon, H. V. Peiris, F. Perrotta, V. Pettorino, F. Piacentini, L. Polastri, G. Polenta, J. L. Puget, J. P. Rachen, M. Reinecke, M. Remazeilles, A. Renzi, G. Rocha, C. Rosset, G. Roudier, J. A. Rubiño-Martín, B. Ruiz-Granados, L. Salvati, M. Sandri, M. Savelainen, D. Scott, E. P. S. Shellard, C. Sirignano, G. Sirri, L. D. Spencer, R. Sunyaev, A. S. Suur-Uski, J. A. Tauber, D. Tavagnacco, M. Tenti, L. Toffolatti, M. Tomasi, T. Trombetti, L. Valenziano, J. Valiviita, B. Van Tent, L. Vibert, P. Vielva, F. Villa, N. Vittorio, B. D. Wandelt, I. K. Wehus, M. White, S. D. M. White, A. Zacchei, and A. Zonca. Planck 2018 results. VI. Cosmological parameters. *A&A*, 641:A6, September 2020.
- <sup>4</sup> Planck Collaboration and P. A. R. et. al. Ade. Planck 2015 results. XIII. Cosmological parameters. *Astronomy & Astrophysics*, 594:A13, October 2016. arXiv:1502.01589 [astro-ph].
- <sup>5</sup> Shadab Alam, Metin Ata, Stephen Bailey, Florian Beutler, Dmitry Bizyaev, Jonathan A. Blazek, Adam S. Bolton, Joel R. Brownstein, Angela Burden, Chia-Hsun Chuang, Johan Comparat, Antonio J. Cuesta, Kyle S. Dawson, Daniel J. Eisenstein, Stephanie Escoffier, Héctor Gil-Marín, Jan Niklas Grieb, Nick Hand, Shirley Ho, Karen Kinemuchi, David Kirkby, Francisco Kitaura, Elena Malanushenko, Viktor Malanushenko, Claudia Maraston, Cameron K. McBride, Robert C. Nichol, Matthew D. Olmstead, Daniel Oravetz, Nikhil Padmanabhan, Nathalie Palanque-Delabrouille, Kaike Pan, Marcos Pellejero-Ibanez, Will J. Percival, Patrick Petitjean, Francisco Prada, Adrian M. Price-Whelan, Beth A. Reid, Sergio A. Rodríguez-Torres, Natalie A. Roe, Ashley J. Ross, Nicholas P. Ross, Graziano Rossi, Jose Alberto Rubiño-Martín, Shun Saito, Salvador Salazar-Albornoz, Lado Samushia, Ariel G. Sánchez, Siddharth Satpathy, David J. Schlegel, Donald P. Schneider, Claudia G. Scóccola, Hee-Jong Seo, Erin S. Sheldon, Audrey Simmons, Anže Slosar, Michael A. Strauss, Molly E. C. Swanson, Daniel Thomas, Jeremy L. Tinker, Rita Tojeiro, Mariana Vargas Magaña, Jose Alberto Vazquez, Licia Verde, David A. Wake, Yuting Wang, David H. Weinberg, Martin White, W. Michael Wood-Vasey, Christophe Yèche, Idit Zehavi, Zhongxu Zhai, and Gong-Bo Zhao. The clustering of galaxies in the completed SDSS-III Baryon Oscillation Spectroscopic Survey: cosmological analysis of the DR12 galaxy sample. *MNRAS*, 470(3):2617–2652, September 2017.
- <sup>6</sup> Timothée Delubac, Julian E. Bautista, Nicolás G. Busca, James Rich, David Kirkby, Stephen Bailey, Andreu Font-Ribera, Anže Slosar, Khee-Gan Lee, Matthew M. Pieri, Jean-Christophe Hamilton, Éric Aubourg, Michael Blomqvist, Jo Bovy, Jon Brinkmann, William Carithers, Kyle S. Dawson, Daniel J. Eisenstein, Satya Gontcho A Gontcho, Jean-Paul Kneib, Jean-Marc Le Goff, Daniel Margala, Jordi Miralda-Escudé, Adam D. Myers, Robert C. Nichol, Pasquier Noterdaeme, Ross O’Connell, Matthew D. Olmstead, Nathalie Palanque-Delabrouille, Isabelle Pâris, Patrick Petitjean, Nicholas P. Ross, Graziano Rossi, David J. Schlegel, Donald P. Schneider, David H. Weinberg, Christophe Yèche, and Donald G. York. Baryon



- acoustic oscillations in the Ly $\alpha$  forest of DR11 quasars. *Astronomy & Astrophysics*, 574:A59, January 2015.
- <sup>7</sup> S. Perlmutter, G. Aldering, G. Goldhaber, R. A. Knop, P. Nugent, P. G. Castro, S. Deustua, S. Fabbro, A. Goobar, D. E. Groom, I. M. Hook, A. G. Kim, M. Y. Kim, J. C. Lee, N. J. Nunes, R. Pain, C. R. Pennypacker, R. Quimby, C. Lidman, R. S. Ellis, M. Irwin, R. G. McMahon, P. Ruiz-Lapuente, N. Walton, B. Schaefer, B. J. Boyle, A. V. Filippenko, T. Matheson, A. S. Fruchter, N. Panagia, H. J. M. Newberg, W. J. Couch, and The Supernova Cosmology Project. Measurements of  $\omega$  and  $\lambda$  from 42 high-redshift supernovae. *The Astrophysical Journal*, 517(2):565–586, June 1999.
- <sup>8</sup> Eleonora Di Valentino, Olga Mena, Supriya Pan, Luca Visinelli, Weiqiang Yang, Alessandro Melchiorri, David F. Mota, Adam G. Riess, and Joseph Silk. In the Realm of the Hubble tension  $\omega$ - $\lambda$  a Review of Solutions, June 2021. arXiv:2103.01183 [astro-ph, physics:gr-qc, physics:hep-ph].
- <sup>9</sup> Wendy L. Freedman. Cosmology at at crossroads: Tension with the Hubble constant, 2017.
- <sup>10</sup> Licia Verde, Tommaso Treu, and Adam G. Riess. Tensions between the early and late Universe. *Nature Astronomy*, 3:891–895, September 2019.
- <sup>11</sup> Eleonora Di Valentino, Luis A. Anchordoqui, Özgür Akarsu, Yacine Ali-Haïmoud, Luca Amendola, Nikki Arendse, Marika Asgari, Mario Ballardini, Spyros Basilakos, Elia Battistelli, Micol Benetti, Simon Birrer, François R. Bouchet, Marco Bruni, Erminia Calabrese, David Camarena, Salvatore Capozziello, Angela Chen, Jens Chluba, Anton Chudaykin, Eoin Ó. Colgáin, Francis-Yan Cyr-Racine, Paolo de Bernardis, Javier de Cruz Pérez, Jacques Delabrouille, Jo Dunkley, Celia Escamilla-Rivera, Agnès Ferté, Fabio Finelli, Wendy Freedman, Noemi Frusciante, Elena Giusarma, Adrià Gómez-Valent, Will Handley, Ian Harrison, Luke Hart, Alan Heavens, Hendrik Hildebrandt, Daniel Holz, Dragan Huterer, Mikhail M. Ivanov, Shahab Joudaki, Marc Kamionkowski, Tanvi Karwal, Lloyd Knox, Suresh Kumar, Luca Lamagna, Julien Lesgourgues, Matteo Lucca, Valerio Marra, Silvia Masi, Sabino Matarrese, Arindam Mazumdar, Alessandro Melchiorri, Olga Mena, Laura Mersini-Houghton, Vivian Miranda, Cristian Moreno-Pulido, David F. Mota, Jessica Muir, Ankan Mukherjee, Florian Niedermann, Alessio Notari, Rafael C. Nunes, Francesco Pace, Andronikos Paliathanasis, Antonella Palmese, Supriya Pan, Daniela Paoletti, Valeria Pettorino, Francesco Piacentini, Vivian Poulin, Marco Raveri, Adam G. Riess, Vincenzo Salzano, Emmanuel N. Saridakis, Anjan A. Sen, Arman Shafieloo, Anwar J. Shajib, Joseph Silk, Alessandra Silvestri, Martin S. Sloth, Tristan L. Smith, Joan Solà Peracaula, Carsten van de Bruck, Licia Verde, Luca Visinelli, Benjamin D. Wandelt, Deng Wang, Jian-Min Wang, Anil K. Yadav, and Weiqiang Yang. Cosmology Intertwined III:  $f\sigma_8$  and  $S_8$ . *Astroparticle Physics*, 131:102604, September 2021.
- <sup>12</sup> Elcio Abdalla, Guillermo Franco Abellán, Amin Aboubrahim, Adriano Agnello, Özgür Akarsu, Yashar Akrami, George Alestas, Daniel Aloni, Luca Amendola, Luis A. Anchordoqui, Richard I. Anderson, Nikki Arendse, Marika Asgari, Mario Ballardini, Vernon Barger, Spyros Basilakos, Ronaldo C. Batista, Elia S. Battistelli, Richard Battye, Micol Benetti, David Benisty, Asher Berlin, Paolo de Bernardis, Emanuele Berti, Bohdan Bilenko, Simon Birrer, John P. Blakeslee, Kimberly K. Boddy, Cleo R. Bom, Alexander Bonilla, Nicola Borghi, François R. Bouchet, Matteo Braglia, Thomas Buchert, Elizabeth Buckley-Geer, Erminia Calabrese, Robert R. Caldwell, David Camarena, Salvatore Capozziello, Stefano Casertano, Geoff C. F. Chen, Jens Chluba, Angela Chen, Hsin-Yu Chen, Anton Chudaykin, Michele Cicoli, Craig J. Copi, Fred Courbin, Francis-Yan Cyr-Racine, Božena Czerny, Maria Dainotti, Guido D’Amico, Anne-Christine Davis, Javier de Cruz Pérez, Jaume de Haro, Jacques Delabrouille, Peter B. Denton, Suhail Dhawan, Keith R. Dienes, Eleonora Di Valentino, Pu Du, Dominique Eckert, Celia Escamilla-Rivera, Agnès Ferté, Fabio Finelli, Pablo Fosalba, Wendy L. Freedman, Noemi Frusciante, Enrique Gaztañaga, William Giarè, Elena Giusarma, Adrià Gómez-Valent, Will Handley, Ian Harrison, Luke Hart, Dhiraj Kumar Hazra, Alan Heavens, Asta Heinesen, Hendrik Hildebrandt, J. Colin Hill, Natalie B. Hogg, Daniel E. Holz, Deanna C. Hooper, Nikoo Hosseinnejad, Dragan Huterer, Mustapha Ishak, Mikhail M. Ivanov, Andrew H. Jaffe, In Sung Jang, Karsten Jedamzik, Raul Jimenez, Melissa Joseph, Shahab Joudaki, Marc Kamionkowski, Tanvi Karwal, Lavrentios Kazantzidis, Ryan E. Keeley, Michael Klasen, Eiichiro Komatsu, Léon V. E. Koopmans, Suresh Kumar, Luca Lamagna, Ruth Lazkoz, Chung-Chi Lee, Julien Lesgourgues, Jackson Levi Said, Tiffany R. Lewis, Benjamin L’Huillier, Matteo Lucca, Roy Maartens, Lucas M. Macri, Danny Marfatia, Valerio Marra, Carlos J. A. P. Martins, Silvia Masi, Sabino Matarrese, Arindam Mazumdar, Alessandro Melchiorri, Olga Mena, Laura Mersini-Houghton, James Mertens, Dinko Milaković, Yuto Minami, Vivian Miranda, Cristian Moreno-Pulido, Michele Moresco, David F. Mota, Emil Mottola, Simone Mozzon, Jessica Muir, Ankan Mukherjee, Suvodip Mukherjee, Pavel Naselsky, Pran Nath, Savvas Nesseris, Florian Niedermann, Alessio Notari, Rafael C. Nunes, Eoin Ó Colgáin, Kayla A. Owens, Emre Özülker, Francesco Pace, Andronikos Paliathanasis, Antonella Palmese, Supriya Pan, Daniela Paoletti, Santiago E. Perez Bergliaffa, Leandros Perivolaropoulos, Dominic W. Pesce, Valeria Pettorino, Oliver H. E. Philcox, Levon Pogosian, Vivian Poulin, Gaspard Poulot, Marco Raveri, Mark J. Reid, Fabrizio Renzi, Adam G. Riess, Vivian I. Sabla, Paolo Salucci, Vincenzo Salzano, Emmanuel N. Saridakis, Bangalore S. Sathyaprakash, Martin Schmaltz, Nils Schöneberg, Dan Scolnic, Anjan A. Sen, Neelima Sehgal, Arman Shafieloo, M. M. Sheikh-Jabbari, Joseph Silk, Alessandra Silvestri, Foteini Skara, Martin S. Sloth, Marcelle Soares-Santos, Joan Solà Peracaula, Yu-Yang Songsheng, Jorge F. Soriano, Denitsa Staicova, Glenn D. Starkman, István Szapudi, Elsa M. Teixeira, Brooks Thomas, Tommaso Treu, Emery Trott, Carsten van de Bruck, J. Alberto Vazquez, Licia Verde, Luca Visinelli, Deng Wang, Jian-Min Wang, Shao-Jiang Wang, Richard Watkins, Scott Watson, John K. Webb, Neal Weiner, Amanda Weltman, Samuel J. Witte, Radosław Wojtak, and Anil Kumar Yadav. Cosmology intertwined: A review of the particle physics, astrophysics, and cosmology associated with the cosmological tensions and anomalies. *Journal of High Energy Astrophysics*, 34:49–211, June 2022.
- <sup>13</sup> Adam G. Riess, Stefano Casertano, Wenlong Yuan, J. Bradley Bowers, Lucas Macri, Joel C. Zinn, and Dan Scolnic. Cosmic distances calibrated to 1% *The Astrophysical Journal Letters*, 908(1):L6, feb 2021.

- <sup>14</sup> H. Hildebrandt, M. Viola, C. Heymans, S. Joudaki, K. Kuijken, C. Blake, T. Erben, B. Joachimi, D. Klaes, L. Miller, C. B. Morrison, R. Nakajima, G. Verdoes Kleijn, A. Amon, A. Choi, G. Covone, J. T. A. de Jong, A. Dvornik, I. Fenech Conti, A. Grado, J. Harnois-Déraps, R. Herbonnet, H. Hoekstra, F. Köhlinger, J. McFarland, A. Mead, J. Merten, N. Napolitano, J. A. Peacock, M. Radovich, P. Schneider, P. Simon, E. A. Valentijn, J. L. van den Busch, E. van Uitert, and L. Van Waerbeke. KiDS-450: cosmological parameter constraints from tomographic weak gravitational lensing. *MNRAS*, 465(2):1454–1498, February 2017.
- <sup>15</sup> H. Hildebrandt, F. Köhlinger, J. L. van den Busch, B. Joachimi, C. Heymans, A. Kannawadi, A. H. Wright, M. Asgari, C. Blake, H. Hoekstra, S. Joudaki, K. Kuijken, L. Miller, C. B. Morrison, T. Tröster, A. Amon, M. Archidiacono, S. Brieden, A. Choi, J. T. A. de Jong, T. Erben, B. Giblin, A. Mead, J. A. Peacock, M. Radovich, P. Schneider, C. Sifón, and M. Tewes. KiDS+VIKING-450: Cosmic shear tomography with optical and infrared data. *A&A*, 633:A69, January 2020.
- <sup>16</sup> Catherine Heymans, Tilman Tröster, Marika Asgari, Chris Blake, Hendrik Hildebrandt, Benjamin Joachimi, Konrad Kuijken, Chieh-An Lin, Ariel G. Sánchez, Jan Luca van den Busch, Angus H. Wright, Alexandra Amon, Maciej Bilicki, Jelte de Jong, Martin Crocce, Andrej Dvornik, Thomas Erben, Maria Cristina Fortuna, Fedor Getman, Benjamin Giblin, Karl Glazebrook, Henk Hoekstra, Shahab Joudaki, Arun Kannawadi, Fabian Köhlinger, Chris Lidman, Lance Miller, Nicola R. Napolitano, David Parkinson, Peter Schneider, HuanYuan Shan, Edwin A. Valentijn, Gijs Verdoes Kleijn, and Christian Wolf. KiDS-1000 Cosmology: Multi-probe weak gravitational lensing and spectroscopic galaxy clustering constraints. *A&A*, 646:A140, February 2021.
- <sup>17</sup> T. M. C. Abbott, M. Aguena, A. Alarcon, S. Allam, S. Allen, J. Annis, S. Avila, D. Bacon, K. Bechtol, A. Bermeo, G. M. Bernstein, E. Bertin, S. Bhargava, S. Bocquet, D. Brooks, D. Brout, E. Buckley-Geer, D. L. Burke, A. Carnero Rosell, M. Carrasco Kind, J. Carretero, F. J. Castander, R. Cawthon, C. Chang, X. Chen, A. Choi, M. Costanzi, M. Crocce, L. N. da Costa, T. M. Davis, J. De Vicente, J. DeRose, S. Desai, H. T. Diehl, J. P. Dietrich, S. Dodelson, P. Doel, A. Drlica-Wagner, K. Eckert, T. F. Eifler, J. Elvin-Poole, J. Estrada, S. Everett, A. E. Evrard, A. Farahi, I. Ferrero, B. Flaugher, P. Fosalba, J. Frieman, J. García-Bellido, M. Gatti, E. Gaztanaga, D. W. Gerdes, T. Giannantonio, P. Giles, S. Grandis, D. Gruen, R. A. Gruendl, J. Gschwend, G. Gutierrez, W. G. Hartley, S. R. Hinton, D. L. Hollowood, K. Honscheid, B. Hoyle, D. Huterer, D. J. James, M. Jarvis, T. Jeltema, M. W. G. Johnson, M. D. Johnson, S. Kent, E. Krause, R. Kron, K. Kuehn, N. Kuropatkin, O. Lahav, T. S. Li, C. Lidman, M. Lima, H. Lin, N. MacCrann, M. A. G. Maia, A. Mantz, J. L. Marshall, P. Martini, J. Mayers, P. Melchior, J. Mena-Fernández, F. Menanteau, R. Miquel, J. J. Mohr, R. C. Nichol, B. Nord, R. L. C. Ogando, A. Palmese, F. Paz-Chinchón, A. A. Plazas, J. Prat, M. M. Rau, A. K. Romer, A. Roodman, P. Rooney, E. Rozo, E. S. Rykoff, M. Sako, S. Samuroff, C. Sánchez, E. Sanchez, A. Saro, V. Scarpine, M. Schubnell, D. Scolnic, S. Serrano, I. Sevilla-Noarbe, E. Sheldon, J. Allyn. Smith, M. Smith, E. Suchyta, M. E. C. Swanson, G. Tarle, D. Thomas, C. To, M. A. Troxel, D. L. Tucker, T. N. Varga, A. von der Linden, A. R. Walker, R. H. Wechsler, J. Weller, R. D. Wilkinson, H. Wu, B. Yanny, Y. Zhang, Z. Zhang, J. Zuntz, and DES Collaboration. Dark Energy Survey Year 1 Results: Cosmological constraints from cluster abundances and weak lensing. *PhRvD*, 102(2):023509, July 2020.
- <sup>18</sup> Xiangchong Li, Tianqing Zhang, Sunao Sugiyama, Roohi Dalal, Ryo Terasawa, Markus M. Rau, Rachel Mandelbaum, Masahiro Takada, Surhud More, Michael A. Strauss, Hironao Miyatake, Masato Shirasaki, Takashi Hamana, Masamune Oguri, Wentao Luo, Atsushi J. Nishizawa, Ryuichi Takahashi, Andrina Nicola, Ken Osato, Arun Kannawadi, Tomomi Sunayama, Robert Armstrong, James Bosch, Yutaka Komiyama, Robert H. Lupton, Nate B. Lust, Lauren A. MacArthur, Satoshi Miyazaki, Hitoshi Murayama, Takahiro Nishimichi, Yuki Okura, Paul A. Price, Philip J. Tait, Masayuki Tanaka, and Shiang-Yu Wang. Hyper Suprime-Cam Year 3 results: Cosmology from cosmic shear two-point correlation functions. *PhRvD*, 108(12):123518, December 2023.
- <sup>19</sup> Gong-Bo Zhao, Marco Raveri, Levon Pogosian, Yuting Wang, Robert G. Crittenden, Will J. Handley, Will J. Percival, Florian Beutler, Jonathan Brinkmann, Chia-Hsun Chuang, Antonio J. Cuesta, Daniel J. Eisenstein, Francisco-Shu Kitaura, Kazuya Koyama, Benjamin L’Huillier, Robert C. Nichol, Matthew M. Pieri, Sergio Rodriguez-Torres, Ashley J. Ross, Graziano Rossi, Ariel G. Sánchez, Arman Shafieloo, Jeremy L. Tinker, Rita Tojeiro, Jose A. Vazquez, and Hanyu Zhang. Dynamical dark energy in light of the latest observations. *Nature Astronomy*, 1(9):627–632, August 2017.
- <sup>20</sup> Nandan Roy. Dynamical dark energy in the light of desi 2024 data, 2024.
- <sup>21</sup> Eleonora Di Valentino, Alessandro Melchiorri, and Olga Mena. Can interacting dark energy solve the  $H_0$  tension? *PhRvD*, 96(4):043503, August 2017.
- <sup>22</sup> Eleonora Di Valentino, Alessandro Melchiorri, Olga Mena, and Sunny Vagnozzi. Interacting dark energy in the early 2020s: A promising solution to the  $H_0$  and cosmic shear tensions. *Physics of the Dark Universe*, 30:100666, December 2020.
- <sup>23</sup> Weiqiang Yang, Supriya Pan, Eleonora Di Valentino, Rafael C. Nunes, Sunny Vagnozzi, and David F. Mota. Tale of stable interacting dark energy, observational signatures, and the  $H_0$  tension. *JCAP*, 2018(9):019, September 2018.
- <sup>24</sup> Li-Yang Gao, She-Sheng Xue, and Xin Zhang. Dark energy and matter interacting scenario to relieve  $H_0$  and  $S_8$  tensions. *Chinese Physics C*, 48(5):051001, May 2024.
- <sup>25</sup> B. Wang, E. Abdalla, F. Atrio-Barandela, and D. Pavón. Further understanding the interaction between dark energy and dark matter: current status and future directions. *Reports on Progress in Physics*, 87(3):036901, March 2024.
- <sup>26</sup> Ji Yao, Huanyuan Shan, Ran Li, Youhua Xu, Dongwei Fan, Dezi Liu, Pengjie Zhang, Yu Yu, Chengliang Wei, Bin Hu, Nan Li, Zuhui Fan, Haojie Xu, and Wuzheng Guo. CSST WL preparation I: forecast the impact from non-Gaussian covariances and requirements on systematics control. *MNRAS*, 527(3):5206–5218, January 2024.
- <sup>27</sup> Marco Baldi. Clarifying the effects of interacting dark energy on linear and nonlinear structure formation processes. *Monthly Notices of the Royal Astronomical Society*, 414(1):116–128, June 2011. arXiv:1012.0002 [astro-ph, physics:gr-qc].

- <sup>28</sup> Jiajun Zhang, Rui An, Shihong Liao, Wentao Luo, Zhaozhou Li, and Bin Wang. A Fully Self-Consistent Cosmological Simulation Pipeline for Interacting Dark Energy Models, November 2018. arXiv:1811.01519 [astro-ph].
- <sup>29</sup> Mark Vogelsberger, Federico Marinacci, Paul Torrey, and Ewald Puchwein. Cosmological Simulations of Galaxy Formation, December 2019. arXiv:1909.07976 [astro-ph].
- <sup>30</sup> Volker Springel. The cosmological simulation code gadget-2. *Monthly Notices of the Royal Astronomical Society*, 364(4):1105–1134, December 2005.
- <sup>31</sup> Volker Springel, Naoki Yoshida, and Simon D.M. White. GADGET: a code for collisionless and gasdynamical cosmological simulations. *New Astronomy*, 6(2):79–117, April 2001.
- <sup>32</sup> Yun Liu, Shihong Liao, Xiangkun Liu, Jiajun Zhang, Rui An, and Zuhui Fan. Dark matter haloes in interacting dark energy models: formation history, density profile, spin, and shape. *Monthly Notices of the Royal Astronomical Society*, 511(2):3076–3088, February 2022.
- <sup>33</sup> W. Zimdahl. Models of Interacting Dark Energy. pages 51–56, 2012. arXiv:1204.5892 [astro-ph, physics:gr-qc, physics:hep-th].
- <sup>34</sup> B. Wang, E. Abdalla, F. Atrio-Barandela, and D. Pavón. Dark matter and dark energy interactions: theoretical challenges, cosmological implications and observational signatures. *Reports on Progress in Physics*, 79(9):096901, September 2016.
- <sup>35</sup> André A. Costa, Xiao-Dong Xu, Bin Wang, Elisa G. M. Ferreira, and E. Abdalla. Testing the Interaction between Dark Energy and Dark Matter with Planck Data. *Physical Review D*, 89(10):103531, May 2014. arXiv:1311.7380 [astro-ph, physics:gr-qc, physics:hep-ph].
- <sup>36</sup> Steffen R. Knollmann and Alexander Knebe. AHF: Amiga’s Halo Finder. *ApJS*, 182(2):608–624, June 2009.
- <sup>37</sup> Shihong Liao. An alternative method to generate pre-initial conditions for cosmological N-body simulations. *MNRAS*, 481(3):3750–3760, December 2018.
- <sup>38</sup> Antony Lewis and Sarah Bridle. Cosmological parameters from CMB and other data: A Monte Carlo approach. *PhRvD*, 66(10):103511, November 2002.
- <sup>39</sup> Martín Crocce, Sebastián Pueblas, and Román Scoccimarro. Transients from initial conditions in cosmological simulations. *MNRAS*, 373(1):369–381, November 2006.
- <sup>40</sup> Peng Wang and Xi Kang. The build up of the correlation between halo spin and the large-scale structure. *Monthly Notices of the Royal Astronomical Society*, 473(2):1562–1569, January 2018.
- <sup>41</sup> Pablo López, Marius Cautun, Dante Paz, Manuel Merchán, and Rien van de Weygaert. Deviations from tidal torque theory: evolution of the halo spin-filament alignment. *Monthly Notices of the Royal Astronomical Society*, 502(4):5528–5545, March 2021. arXiv:2012.01638 [astro-ph].
- <sup>42</sup> Peng Wang, Quan Guo, Xi Kang, and Noam I. Libeskind. The spin alignment of galaxies with the large-scale tidal field in hydrodynamic simulations. *The Astrophysical Journal*, 866(2):138, October 2018. arXiv:1810.04581 [astro-ph].
- <sup>43</sup> Francisco Villaescusa-Navarro. Pylians: Python libraries for the analysis of numerical simulations. Astrophysics Source Code Library, record ascl:1811.008, November 2018.